CHAPTETR 2

Literature review

This chapter presents the background information which includes dielectricity, relaxor ferroelectricity, and perovskite materials with relaxor behavior. It is necessary to describe the general background of $Ba_{0.85}Ca_{0.5}Zr_{0.1}Ti_{0.9}O_3$ (BCZT). Moreover, previous works have investigated different synthesis methods of BCZT powder and various dopants. Therefore, the information will also be mentioned in the following part.

2.1 Dielectricity

2.1.1 Dielectric constant

Dielectricity is the property of a material in which an applied electric field produces internal polarization. It has important parameters such as dielectric constant or relative permittivity (ε_r) and dielectric loss or loss tangent ($tan\delta$). The following equation describes the total charge neutrality of material under an external electric field,

$$D = \varepsilon_0 E + P \tag{2.1}$$

where the $\varepsilon_0 E$ is the vacuum contribution caused by applying the external electric field, and, P is the electrical polarization in the material.

For the material which has a pure dielectric response, the polarization is proportional to the electric field in a linear approximation by

$$P = \varepsilon_0 \chi_e E \tag{2.2}$$

where the χ_e is the electrical susceptibility.

Substituting put Equation (2.2) in (2.1), then

$$D = \varepsilon_0 E + \varepsilon_0 \chi_e E$$

$$D = (1 + \chi_e)\varepsilon_0 E \tag{2.3}$$

If the space between 2 plates is filled by a material having the electrical susceptibility χ_e, increase of the capacitance depends on the factor of $1+\chi_e$.

The dielectric permittivity ε is defined by

$$\varepsilon = \varepsilon_0(1+\chi_e) \tag{2.4}$$

where

$$\varepsilon_r = \frac{\varepsilon}{\varepsilon_0} = 1+\chi_e \tag{2.5}$$

ε_r is the relative permittivity or dielectric constant of material.

2.1.2 Dielectric loss

Dielectric loss ($tan\delta$) is a current-voltage relationship for charging and discharging a capacitor, which is defined by using the phasor diagram (Fig. 2.1). When a perfect capacitor is under an external alternating electrical field shown in Fig. 2.1(a), the instantaneous current (I_c) (as a vertical line) has a phase difference compared to the voltage (U) (as a horizontal line) by 90º. For a real capacitor presented in Fig. 2.1(b), the phase difference between current and voltage is less than 90º.

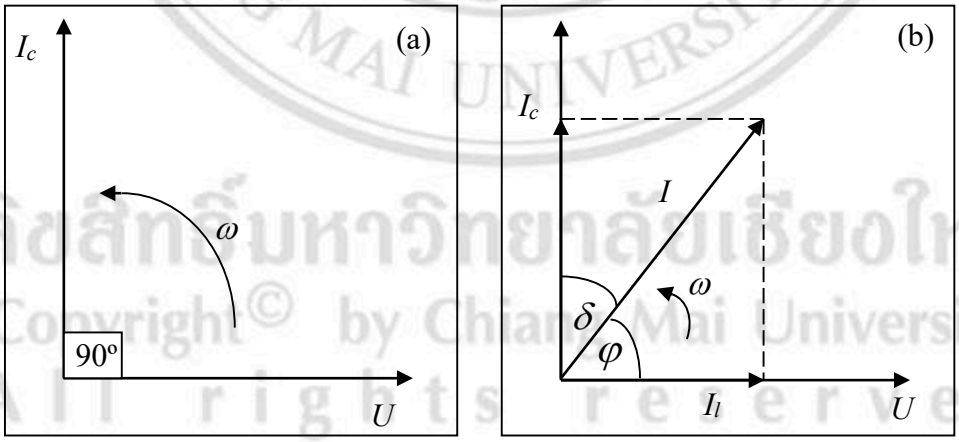

Figure 2.1 Modified phasor diagram of (a) a perfect capacitor and (b) a real capacitor [24].

If there is a next extraction of power by a source, there must be a component I_l of I in phase with U as shown in Fig. 2.1(b), which it leads to power loss, while a I_c does not. Thus a time average power is define by

$$\bar{P} = \frac{1}{T}\int_0^T UIdt \tag{2.6}$$

then,

$$\bar{P} = \frac{1}{T}\int_0^T U_0 \sin(\omega t) I_0 \cos(\omega t - \delta) dt \tag{2.7}$$

integrating Equation (2.7) gives

$$\bar{P} = \frac{1}{2} U_0 I_0 \sin\delta \tag{2.8}$$

since $I_0 = I_C \cos\delta$ and $I_C = \omega U_0 C$,

$$\bar{P} = \frac{1}{2} U_0 I_0 \tan\delta = \frac{1}{2} U_0^2 \omega\varepsilon C \tan\delta \tag{2.9}$$

$U_0/\sqrt{2}$ and $I_0/\sqrt{2}$ are a root mean square (rms) voltage and a rms current, respectively. From Equation (2.9) can be seen that "dissipation factor" or $tan\delta$ is a relationship between a fraction of the capacitive current (the component in the degree of 90º and out of phase with the voltage) and a voltage, dissipated as heat.

Substitutions of U_0, C and Ah by $E_0 h$, $\varepsilon_r \varepsilon_0 A/h$ and V, respectively, lead to an equation for a dissipated power density in a dielectric,

$$\frac{\bar{P}}{V} = \frac{1}{2} E_0^2 \omega\varepsilon_0 \varepsilon_r C \tan\delta \tag{2.10}$$

$\varepsilon_r \tan\delta$ is a loss factor of a dielectric and $\omega\varepsilon_0\varepsilon_r C tan\delta$ is a dielectric conductivity.

Since behavior of an alternative current circuit is analyzed to be a complex quality. A complex permittivity of dielectric supposes to be mentioned as the following equation as,

$$\varepsilon_r^* = \varepsilon_r' - j\varepsilon_r'' \tag{2.11}$$

where a real and an imaginary parts of dielectric are defined as ε_r' and ε_r'', respectively. For a real dielectric applied with an alternative current field, a current passed through a dielectric is made up of two components, one capacitive which is "lossless" and "lossy" which is the other in phase with *U*, as shown in Fig.2.2 It can be seen from Fig. 2.2 that

$$\frac{\varepsilon_r''}{\varepsilon_r'} = \tan\delta \tag{2.12}$$

where $tan\delta$ is a dissipation factor or dielectric loss.

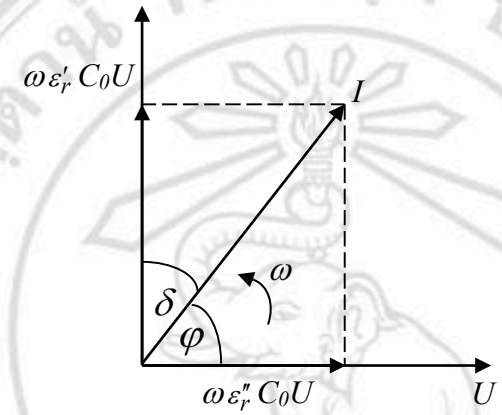

Figure 2.2 Phasor diagram showing "lossless" (capacitive) and "lossy" components of total current *I* [25].

2.1.3 Frequency dependence of dielectric polarization

Frequency dependences of real and imaginary parts of dielectric for each polarization process are shown in Fig.2.3. The polarization process involve 4 mechanisms as shown in Fig.2.4. First, space charge mechanism which is related to the diffusion of all ions in the grain after applied an electric field, the new alignment of charge happen in the grain boundary. Second, dipolar mechanism, the random dipoles transform to the same direction of dipoles under electric field. Third, the small displacement of ions from external electric field and finally, atomic mechanism which involves the electron are around atom and separate from the centre under application of an electric filed.

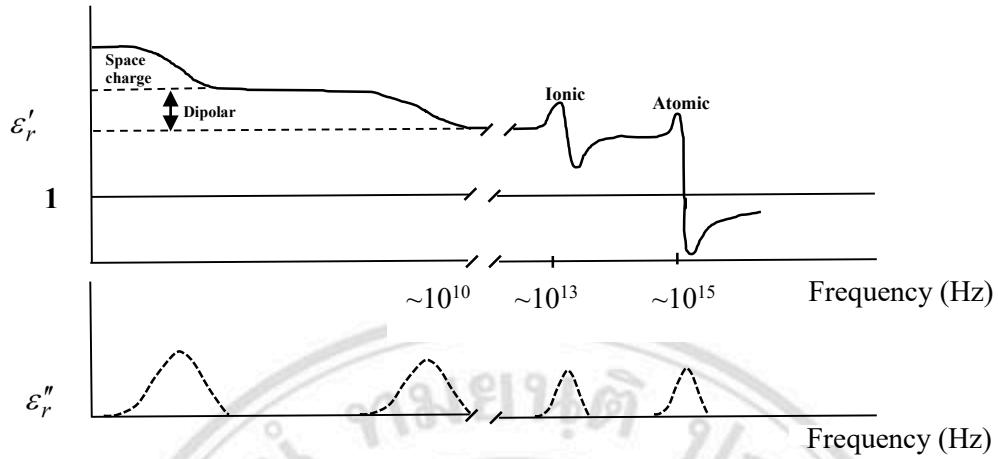

Figure 2.3 Frequency dependences of real and imaginary parts of dielectric for each polarization process [25].

Polarization process	Unpolarized state	Polarized state	Frequency (Hz)
Space charge or diffusional	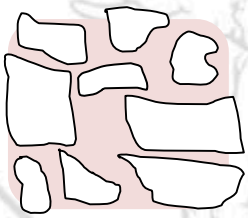	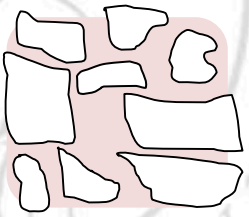	10^{-2}-10^{2}
Dipolar	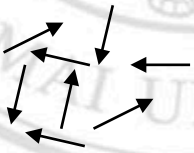	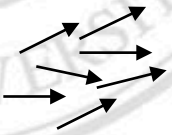	10^{2}-10^{6}
Ionic	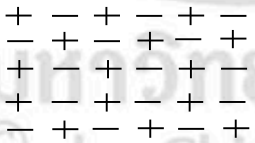	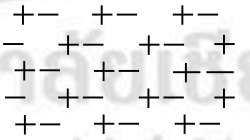	10^{6}-10^{12}
Atomic	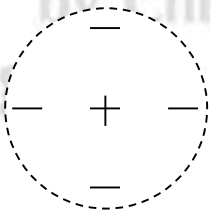	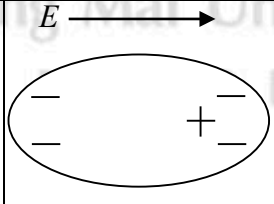	10^{12}-10^{16}

Figure 2.4 Polarization processes with unpolarized and polarizaed state [25].

2.2 Ferroelectric properties

2.2.1 Ferroelectric phases and domains

In 1921, Valasek discovered ferroelectricity in Rochelle salt [26]. The ferroelectric phase is a state that shows spontaneous polarization which can be reoriented by applying an external electric field. Different crystal structures usually have different directions of individual spontaneous polarization as illustrated in Fig 2.5. The alignment of electric dipole in material can occur in both uniform orientation and non-uniform orientation which relates to the reverse direction i.e. in twining. The area in which the uniform polarization exists is called “ferroelectric domain” while the interface between adjacent domains is called “the domain wall”. In general, the effects of the defect and mechanical stress can result in the formation of domain in order to minimize the electrostatic energy of the system. Fig. 2.6 shows the 90° and 180°domains in a tetragonal ferroelectric perovskite.

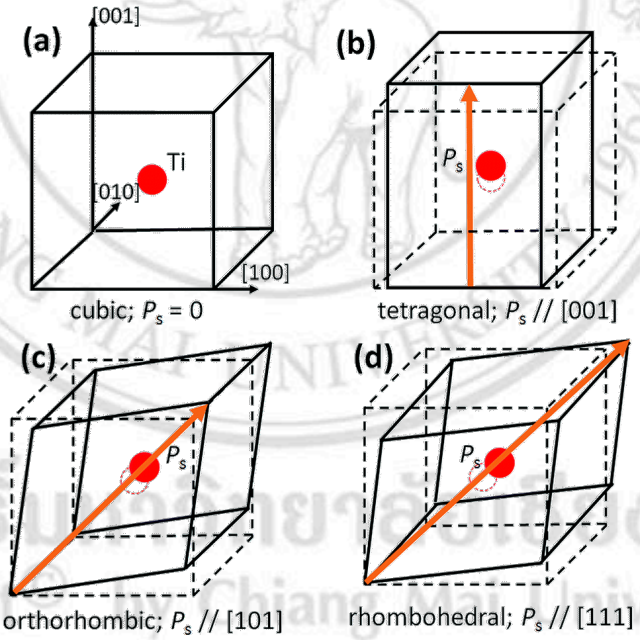

Figure 2.5 Unit cells and the Ti displacement in four $BaTiO_3$ phases (a) cubic, (b) tetragonal, (c) orthorhombic, and (d) rhombohedral. Arrows indicate the spontaneous polarization (P_s) orientations in each phase [27].

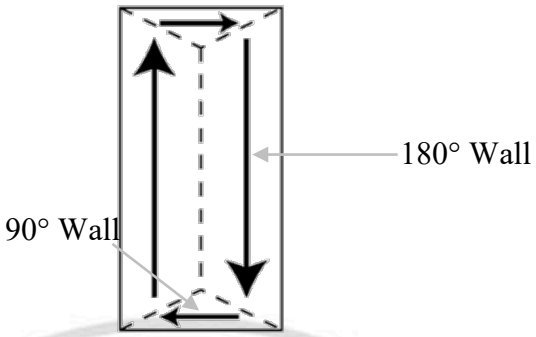

Figure 2.6 A schematic illustration of ferroelectric domains having 90° and 180° oreintations in a tetragonal ferroelectric perovskite [28].

2.2.2 Polarization switching and hysteresis loop

When an external electric field is applied, the domain wall movement can produce single domain. The polarization within the domain can be switched by high enough applied external electric field. A measurement of the hysteresis polarization (P) as a function of electric field (E), called *P-E* hysteresis loop using a simple circuit described by Sawyer-Tower [29], can display ferroelectricity in the materials. This polarization mechanism being with the segment OA of the *P-E* loop in Fig 2.7. As the external electric field strength increases, the domains orientated in other directions will switch towards the direction of the electric field, which results in a rapid increment in polarization magnetude (i.e. segment AB). After that, nearly all domains are aligned and reach a saturation state in segment BC. At this state, properly oriented crystal will be composed of a single domain. When the external electric field strength is decreased, the polarization will decrease as segment BD but it does not go back to the origin. When the external electric field is reduced to zero, a remnant polarization (P_r) is present at this state and relates to the remaining of aligned domains. The extrapolation of the linear segment BC of the hysteresis loop back to polarization axis indicates the spontaneous polarization (P_s) shown as CBE line. When the external electric field is in the opposite direction at point F, the remnant polarization cannot be completely removed. The coercive field (E_c) is required to reduce the polarization back to zero. Further, the increasing electric filed in more negative direction again causes the alignment of the dipoles in this direction and the cycle is completed. Therefore, the relation between *P* and *E* is a representative of the hysteresis loop (CDFGHC) shown in Fig. 2.7 [30, 31]. However, some of ferroelectric ceramics are not good insulator due to contribution of their conductivity and high loss.

The hysteresis loop behavior of these ceramics is presented in Fig. 2.8 which has an elliptical shape.

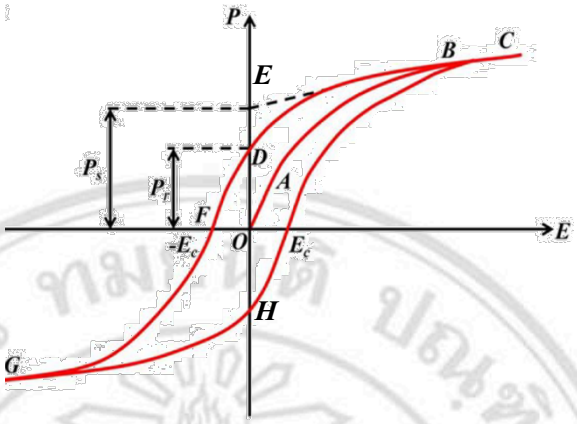

Figure 2.7 A typical *P-E* hysteresis loop in ferroelectric materials [30, 31].

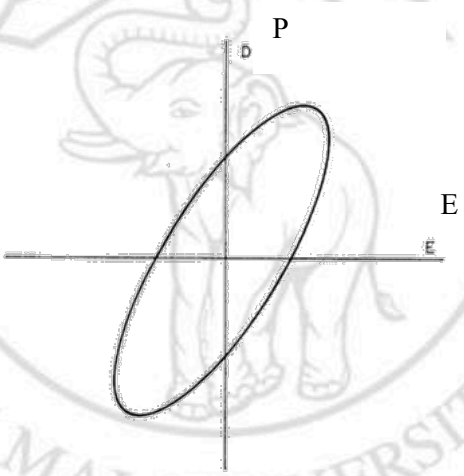

Figure 2.8 Hysteresis loop for a lossy capacitor [32].

2.3 Relaxor ferroelectricity

Relaxor ferroelectric, such as $Pb(Mg_{1/3}Nb_{2/3})O_3$, $BaTiO_3$-$BaSnO_3$ system [33], $K_{0.5}Na_{0.5}Nb_{0.5}$-based (KNN-based), $Bi_{0.5}Na_{0.5}TiO_3$-based (BNT-based) and $Ba_{0.85}Ca_{0.15}Zr_{0.1}Ti_{0.9}O_3$ [34, 35, 36, 37] have received much attention in the fields of material science and physics about their nanostructural and dielectric properties [9,10,38,39]. It has 3 characteristics which are different from normal ferroelectric materials.

1. Relaxor materials present a broad maximum of the relative permittivity compared to normal ferroelectric materials which show a sharp peak of dielectric permittivity vs temperature as shown in Fig. 2.9. The maximum temperature (T_{max}) in relaxor material

also depends on frequency such that the value increases with increasing frequency. In contrast, no frequency dependence of Curie temperature (T_c).

2. The unusually high dielectric permittivity of relaxor ferroelectrics is produced by the local polarization and nano-sized domains. They nucleate and grow at below Burns temperature (T_B) which is higher than T_m. On the other hand, normal ferroelectric has high dielectric permittivity arises from an increase in lattice polarization near the ferroelectric phase transition with accompanying change in symmetry.

3. No macroscopic ferroelectric phase transition when a relaxor is cooled below the maximum temperature. No macroscopic polarization or birefringence develops spontaneously but it is possible to induce a macroscopic polar phase by applying an external electric field at low enough and lower than the depolarization temperature (T_d). The definition of T_d is the highest temperature that an applied external electric field can induce a macroscopically polar state.

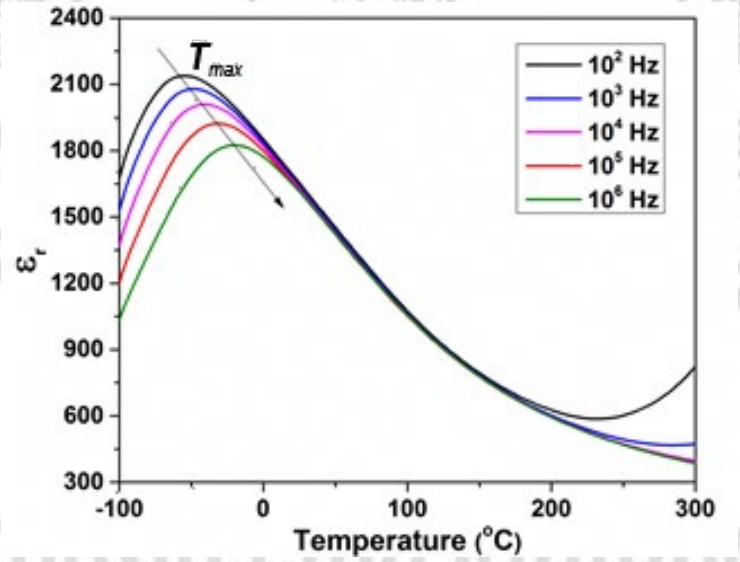

Figure 2.9 Dielectric permittivity as a function of temperature and frequency for relaxor ferroelectric material.

The dielectric properties of relaxor ferroelectric materials are believed to be involved with the crystal chemistry and nanostructure. Many lead-based relaxor systems are complex perovskite with the $Pb\left(B'_yB''_{1-y}\right)O_3$ formula in which the disordered B' and B'' ions are distributed along crystallographically equivalent octahedral sites [9, 10]. Smolenski et al. first reported that the chemical inhomogeneity of the B' and B'' ions created the difference

in local Curie temperature (T_c) and spreaded out the phase transition over a range of temperature and, hence, T_{max} represents the average value of T_c [40]. A superparaelectric model for relaxor ferroelectrics materials was proposed by Cross through an analogy with a superparamegnetic state [9]. This model reports that the micro polar regions are being dynamically disordered by thermal activation among different polarization states at high temperature. The height of the activation energy barrier between domain states is directly proportional to the volume of the polar region. Upon cooling, the activation energy of those regions is less than their kT (k is a Boltzman constant ~1.38064852 × 10^{-23} m^2 kg s^{-2} K^{-1}) and they will be frozen into a preferential orientation which is related to a state of ferroelastic to form a polar microdomain.

After that, Viehland and Cross studied in more details about their model. They described that the dispersion of T_{max} in terms of an alternative current measurement frequency (ω) by a Vogel-Fulcher (VF) law [11],

$$\omega = \omega_0 \exp\left[\frac{-E_a}{T_{\max} - T_{VF}}\right] \tag{2.6}$$

where, ω_0 is the Debye frequency,

E_a is the activation energy,

T_{VF} is the freezing temperature which is very close to T_d.

The mechanism for a relaxor behavior is proposed to be originated from the frustration of different interactions between unit cells. The direction of spontaneous displacement of a certain ion from high symmetry position in ferroelectric is controlled by the balance of elastic and dipole-dipole forces. The determination of these forces can be calculated by the composition of the unit cells surrounding the ions. For example, complex perovskites with different cations oriented in order on equivalent sites usually exhibit antiferroelectric (AFE) ordering, whereas in disordered perovskites, no type of ordering is observed. The degree of ordering is related to the relative difference in valence, ionic radius and stoichiometry. For example, if there is a large difference in radius of cation, AFE ordering will be fovored in order to reduce elastic strain in the structure. However, the long range ordering is not observed in those complex pervoskites and only ferroelectric or relaxor properties are displayed. One example of complex perovskite is $Pb(Mg_{1/3}Nb_{2/3})O_3$ or PMN which is known to be a prototype relaxor ferroelectric material. The mechanism of this system is believed to originate from heterogeneous distribution of the cations (Mg^{2+}

and Nb^{5+}). The uneven distribution is due to the 2:1 stoichiometry between the two different ions, which inhibit long range ferroelectric order. Instead of macroscopic domains, polar nano-regions (PNRs) form in the regions rich in one type of ion.

The previous microscopic model was further extended by Bokov and Ye, who proposed a soft polar nanoregion model [13,14]. This model reported that, at high temperature, the ralaxors exist in a non-polar paraelectric (PE) state, which is similar to normal ferroelectric. Upon cooling, they transform into an ergodic relaxor (ER) state which contains small size and randomly distributed PNRs. This transformation occurrs at the Burn temperature (T_B) and an ion in sublattices of the perovkite structure displaces from high symmetry position, which is determined by a composition of a unit cell surrounding an ion as a local spontaneous polarization P as shown in Fig. 2.10. Considering the structural phase transition, no change of crystal structure on a macroscopic or mesoscopic scale is observed.

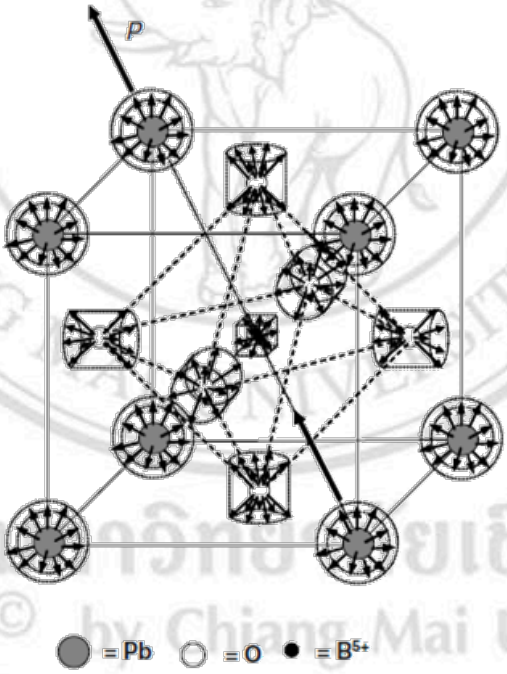

Figure 2.10 Local spontaneous polarization P as shown by thick arrows caused by the correlated displacement of ion inside PNRs, in a unit cell of the lead complex perovskite relaxor. Small arrows present typical uncorrelated ion displacements [41].

The chemical composition surrounding an ion controls the direction of local spontaneous polarizations. Thus, the direction of polar nano regions (PNRs) is also controlled by local spontaneous polarization. For example, focusing on B' and B'' ions, an ion encircled by

its same ion would prefer ferroelectric ordering. However, an ion surrounded by different ions would prefer antiferroelectric ordering. In a chemically disordered configuration, the parts rich in one type of ion would have interactions very strong that their individual polarizations are fixed thus they can be only reoriented by applying an external electric field. These cells are called “fixed cells”. Conversely, in the case of an intermediate concentration of each of neighbor, there will be frustration between ordering of ferroelectric and antiferroelectric, and the cell will be free to fluctuate with thermal activation. These cells are called “free cells”. The dipole moment of free cells can switch from one potential well to another. The schematic of the composition dipole arrangement of B' and B'' ions and dipole moment of PNRs is shown in Fig. 2.11.

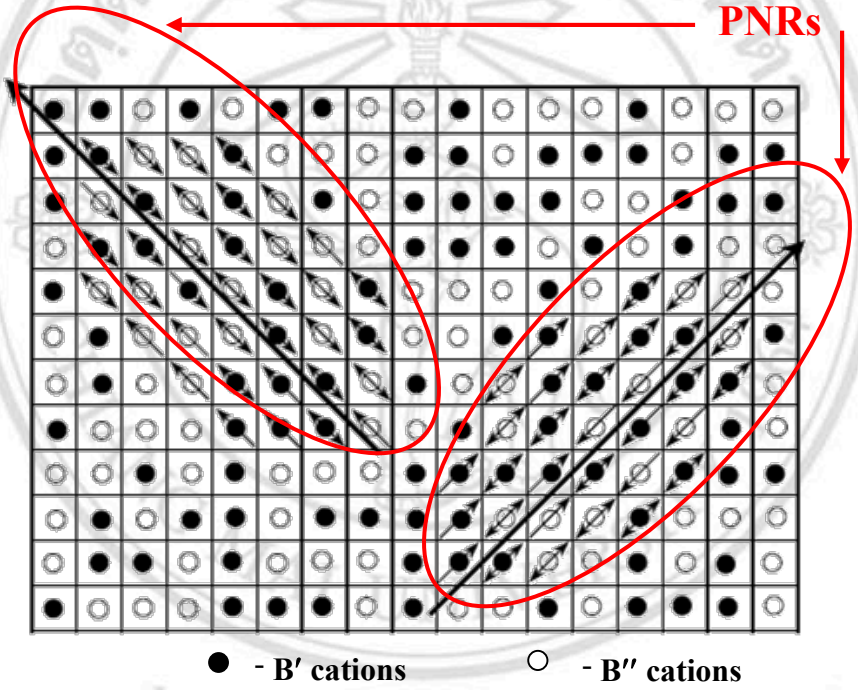

Figure 2.11 Schematic representation of the soft polar nanoregion model discovered by Bokov and Ye for compositionally disordered A(B′B″)O_3 perovskites. A and O ions are not shown. One-way and two-way small arrows represent spontaneous dipole moments of fixed cells and free cells, respectively. Large arrows represent the polarization of the individual PNRs [14].

The PNRs start to nucleate as the temperature decreases to T_B. Their size and number increase when the temperature further decreases, leading to the increase in dielectric permittivity. Upon further cooling, the dynamic of PNRs begin to slow down, leading to a decrease in the permittivity. This creates a permittivity peak and the temperature where this place occurs is called T_{max}. In this model, the temperature between T_{max} and T_B

involves the thermally activated reorientation of dipole moment within PNRs which allow for direction and magnitude of polarization with time. This would indicate two polarization mechanisms: one is related to the reorientation of the dipole moments of PNRs and is called the "conventional relaxor (CR)" contribution, and the other is related to the magnitude of polarization dependent on the time, called the universal relaxor (UR) contribution [41] as shown in Fig. 2.12.

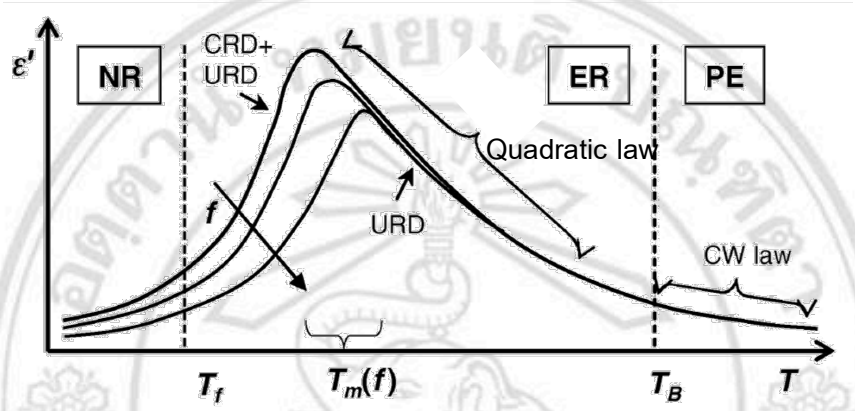

Figure 2.12 Schematic representation of temperature evolutions of the structure and dielectric properties in compositionally disordered perovskite. There are three types of structures i.e. paraelectric (PE), ergodic relaxor (ER) and nonergodic relaxor (NR). When the temperature is higher than T_B, the Curie-Weiss (CW) law applies. For the temperature lower than T_B to T_{max}, the Quadratic law can be used. As the temperature decreases to lower than T_f, the behavior follows by Volgel-Fulcher law. The regions of conventional relaxor dispersion (CRD) and universal relaxor dispersion (URD) are identified [41].

Therefore, the permittivity in the range of temperature above T_{max} for PMN and many relaxors was successfully modeled by a quadratic law [42]

$$\frac{\varepsilon_A}{\varepsilon} = 1 + \frac{(T - T_A)^2}{2\delta^2} \tag{2.7}$$

where, T_A is the temperature lower than T_{max} and is a parameter defining a highest ideal temperature in relaxors,

ε_A is an extrapolated value the a permittivity at T_A,

δ is a degree of diffuseness of the permittivity peak in relaxors.

It was found that this equation could fit to a large number of relaxors with different degrees of diffuseness.

As temperature is further decreased below T_{max} to a certain temperature, so-called a freezing temperature (T_f), the PNRs begin to freeze in some preferred orientation direction. This state is called the nonergodic relaxor (NR) state. This state cannot be reversibly transformed to the phase with ferroelectric dipole order with a critical strength of an applied external electric field (E_{cr}). A degree of the induced ferroelectric phase in the NR state depends on a chemical composition within the materials. For example, the ZnO addition in PMNT ceramics could enhance the degree of ferroelectric order while decrease the degree of relaxor behavior [43].

At high temperature more than T_B, the relaxors exhibit a paraelectric behavior and can be described by the "Curie-Weiss" law,

$$\varepsilon' = \frac{C}{(T - T_{CW})} \tag{2.8}$$

where, C is the Curie-Weiss constant,

T_{CW} is the Curie-Weiss temperature.

2.4 Lead-free perovskite materials

Most of ferroelectric materials are based on the perovskite structure which has the general formula of ABO_3. In addition, this structure has been studied in many years such as lead zirconate titanate ($Pb(Zr_xTi_{1-x})O_3$), lead magnesium niobate titanate ($PbMg_xNb_{2x}Ti_{1-3x}O_3$), barium titanate ($BaTiO_3$)], barium zirconium titanate ($Ba(Zr_xTi_{1-x})O_3$) [13, 14, 44, 45]. However, lead-based pervoskite materials are of concerns to the environment and human health. Thus, lead-free perovskite materials are one of the solutions to these problems. In this work, it is appropriate to present the background of barium calcium zirconate titanate ((1-x)BCT-xBZT) ceramic.

2.4.1 Barium calcium zirconate titanate ((1-x)BCT-xBZT)

The $(1-x)(Ba_{0.7}Ca_{0.3})TiO_3$-$xBa(Zr_{0.2}Ti_{0.8})O_3$ or (1-x)BCT-xBZT system has been previously reported in 2009 by Liu and Ren [15]. They exists a triple point cubic ($Pm\bar{3}m$), rhombohedral ($R3m$) and tetragonal ($P4mm$) in the phase diagram locating at $x \sim 32\%$ and at the temperature of 57ºC. This point is similar to the MPB points of the high-

performance lead-based systems such as lead zirconate titanate (PZT) and lead magnesium niobate titanate (PMNT) [46]. The phase diagram of BZT-*x*BCT system is presented in Fig.2.13. There are three noted compositions in this system, i.e. 20BCT-80BZT, 50BCT -50BZT and 90BCZT-10BZT, respectively. The composition of 50BCT-50BZT or BCZT exhibits excellent properties such as highest remnant polarization (P_r) ~20 μc/cm^2, lowest coercive field (E_c) ~0.016 kV/cm, highest dielectric permittivity (ε_r) ~3060, highest piezoelectric constant (d_{33}) ~620 pC/N and highest the converse piezoelectric coefficient (dS/dE) ~1140 pm/V. These properties in BCZT system are comparable to the properties of PZT and PMN-PT system. However, the phase diagram of BCZT system was revised by Keeble et al. They reported that it also had an intermediate orthorhombic phase (*Amm2*) at room temperature as shown in Fig.2.14. Thus, they showed the succession of 3 phase transitions for 50BCT-50BZT [47]. The high-resolution synchrotron X-ray diffraction techniques have been used in their work.

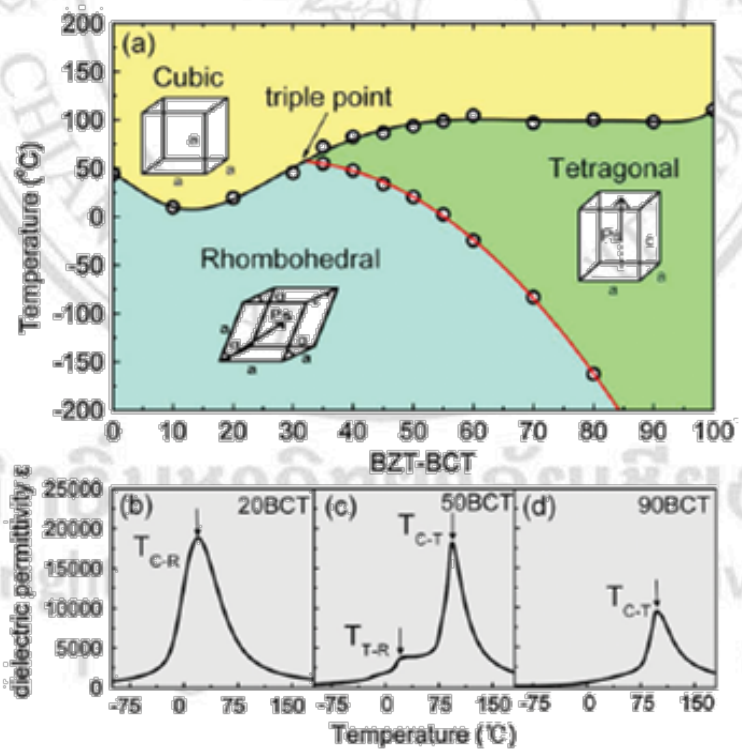

Figure 2.13 (a) Phase diagram of pseudobinary ferroelectric $Ba(Zr_{0.2}Ti_{0.8})O_3$-$x(Ba_{0.7}Ca_{0.3})TiO_3$ or BZT-*x*BCT system (b)-(d) the temperature dependence of dielectric permittivity of 80BZT-20BCT, 50BZT-50BCT and 10BZT-90BCZT, respectively [15].

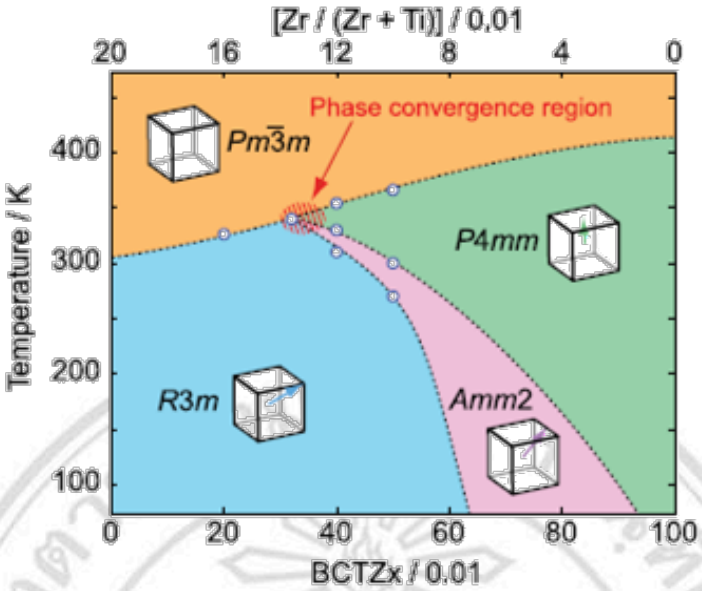

Figure 2.14 Modified phase diagram of pseudobinary ferroelectric $Ba(Zr_{0.2}Ti_{0.8})O_3$-$x(Ba_{0.7}Ca_{0.3})TiO_3$ or BZT-xBCT system [47].

Wang et al [16] reported an optimized calcination temperature of 1300ºC and sintering temperature of 1540ºC of the BCZT ceramic, which also exhibited excellent dielectric properties (ε_r ~4500 and $tan\delta$ <0.009). The increase in $tan\delta$ values with increasing the calcination and sintering temperatures was thought to be due to the generated oxygen vacancies at high temperature. In addition, the large grain size from increasing the sintering temperatures could improve the dielectric properties similar to other lead-free system such as potassium sodium niobate (KNN) and bistmuth titanate (BNT) as shown in Fig.2.15.

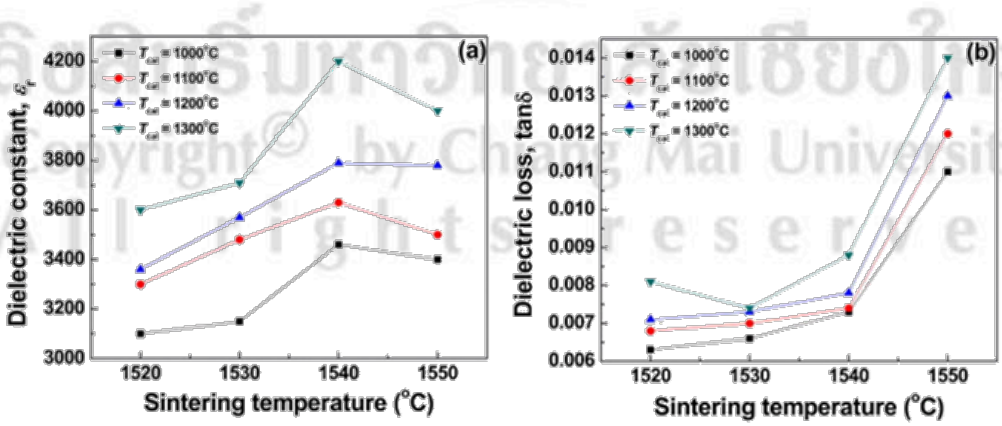

Figure 2.15 Dielectric properties as a function of sintering temperature (a) dielectric permittivity and (b) dielectric loss of BCT-BZT ceramics [47].

Rafig et al [48] reported a BCZT powder calcined at 1350ºC and a high ceramic density was obtained by sintering at 1500ºC. The lattice parameters were calculated after refinement of the XRD pattern by FullProf software, in which a = 4.009 Å and c = 4.036 Å, in a tetragonal perovskite structure as presented in Fig.2.16. They also reported a high ε_r of ~12,100 at the transition temperature. The increase of the sintering temperature could increase the grain size leading to an improvement of the dielectric properties. They suggested that the large grain sizes had a strong insulating layer around the grains and promoted an easier domain wall motion. The phase transition temperature was observed at 105ºC and it depended on grain size and cell distortion.

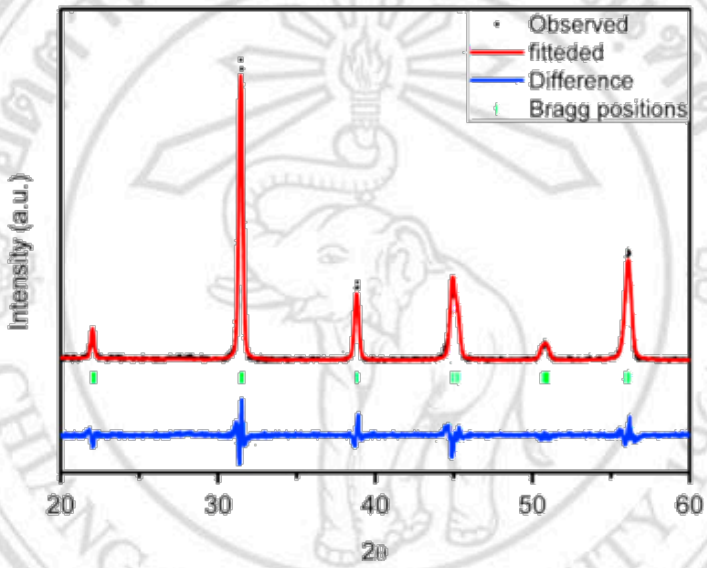

Figure 2.16 Refinement of the XRD pattern of BCZT ceramic sintered at 1500ºC [48].

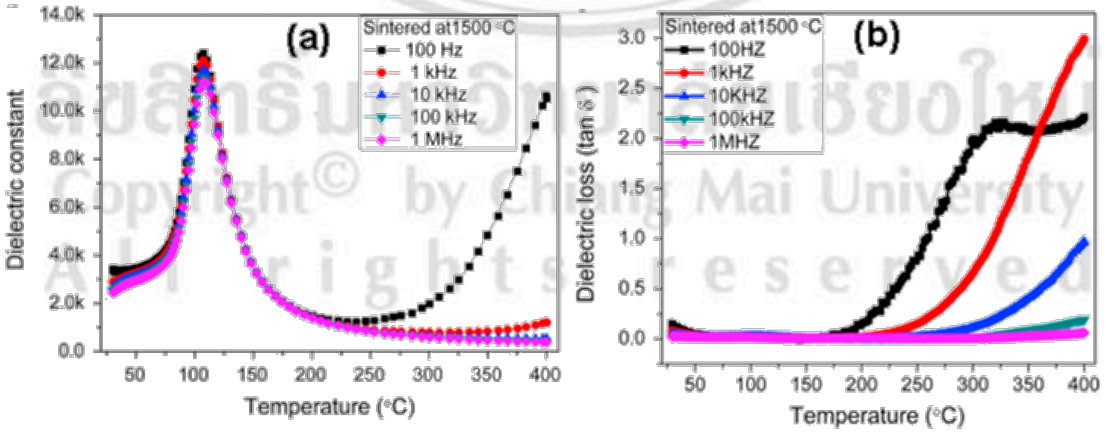

Figure 2.17 Dielectric properties as a function of temperature and frequencies (a) dielectric permittivity and (b) dielectric loss of BCZT ceramic sintered at 1500ºC [48].

Wu et al [49] have studied the effect of dwell time during sintering on properties of BCZT ceramics. They found that the optimum dwell time of 5 h (1500ºC) could improved the properties. The dielectric curves presented two peaks which colud be assigned to rhombohedral to tetragonal and tetragonal to cubic phases as shown in Fig. 2.18. Saturated hysteresis loops were observed for all ceramics and $2P_r$ values tended to increase with increasing dwell time (see Fig. 2.19).

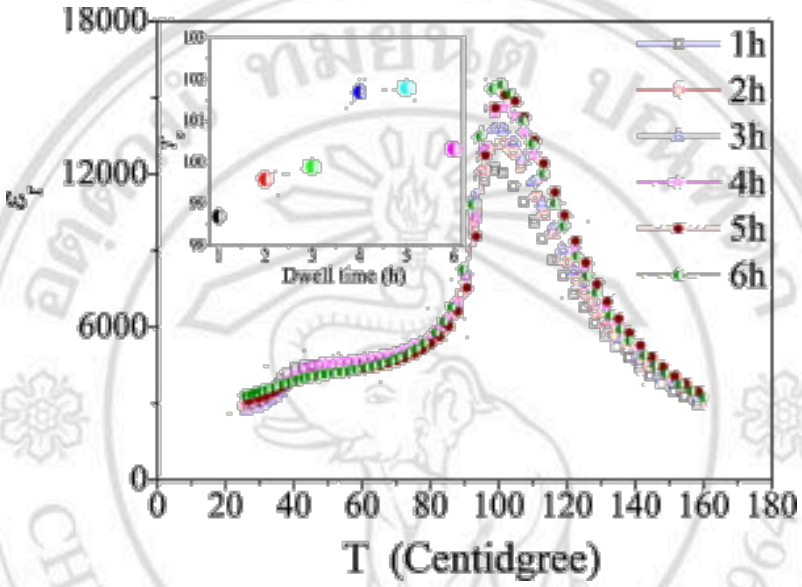

Figure 2.18 Temperature dependence of dielectric permittivity of BCZT ceramics with various dwell times during sintering and Curie temperature versus dwell time [49].

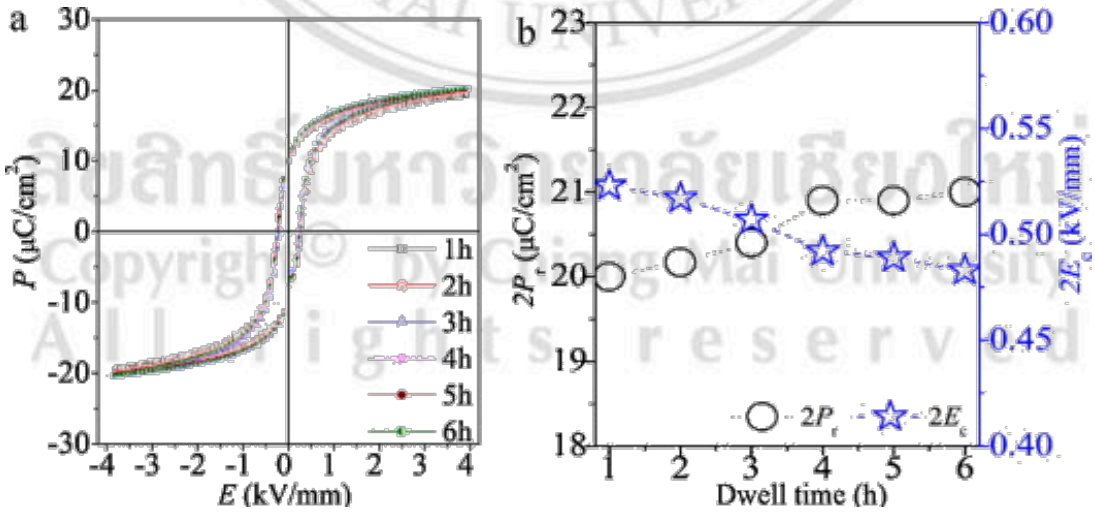

Figure 2.19 Hysteresis loops (left) and $2P_r$ and $2E_c$ of BCZT ceramics with various dwell times [49].

Hence, the BCZT ceramic prepared a high calcinations and sintering temperature (1300ºC and 1500ºC) showed excellent ferroelectric and dielectric properties. Thus, this ceramic therefore is of interest for development. Different dopants have been used for the development of BCZT ceramic. Wu et al [50] studied a modification of BCZT ceramic by ZnO addition. The BCZT powder and ceramics were prepared at 1200ºC and 1480ºC, respectively. The results showed that the grain size and densities increased by small addition of ZnO because the Zn^{2+} substituted into the $(Ti, Zr)^{4+}$ site led to the oxygen vacancy generation which helped the mass transport in the sintering process (see Fig 2.20). The ZnO addition at 0.06 mol% presented a good processing condition with ε_r ~4500, $tan\delta$<1.5% and $2P_r$ ~ 19.37 μC/cm^2 as shown in Fig.2.21.

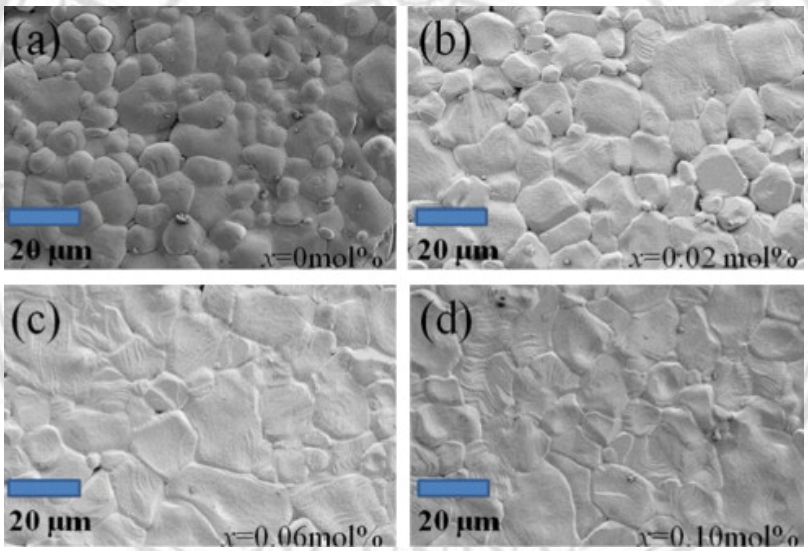

Figure 2.20 SEM images of BCZT ceramics with various ZnO additions where (a) 0 mole% (b) 0.02 mole% (c) 0.06 mole% and (d) 0.10 mole%, respectively [50].

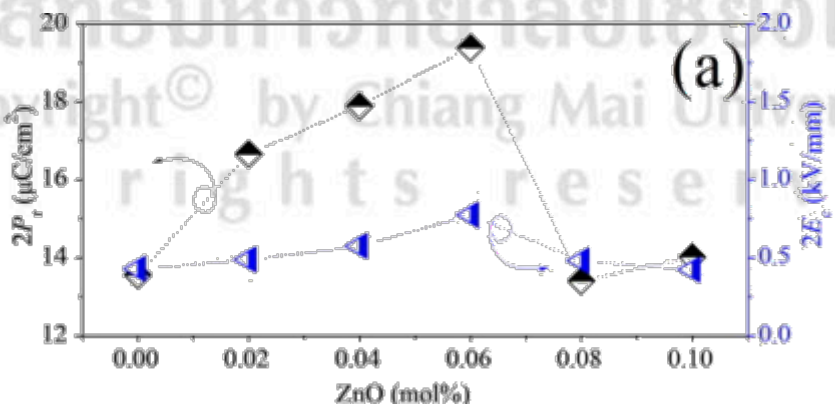

Figure 2.21 $2P_r$ and $2E_c$ with difference of ZnO additions in BCZT ceramics [50].

Cui et al [51] reported the effect of CuO addition on the properties of BCZT ceramics. They successfully prepared the ceramics at a low sintering temperature of 1350ºC. They reported that the phases of BCZT-*x*CuO ceramics (x = 0.04-0.06 wt%) were consisted of tetragonal and rhombohedral phases at room temperature. The composition of BCZT-*0.04*wt%CuO presented highest ε_r and lowest $tan\delta$ values as shown in Fig. 2.22. It was mentioned that the observed good properties should be obtained in the sample with two-phase coexistence. They also studied the effect of Y_2O_3 [52] addition in the BCZT ceramic. They reported that the ceramics were also prepared at 1350ºC and the results showed that the grain sizes were developed by Y_2O_3 addition as shown Fig. 2.23. Small amount of Y_2O_3 addition in the BCZT ceramic caused T_C to increase from 85ºC to 95ºC which is shown in Fig 2.24.

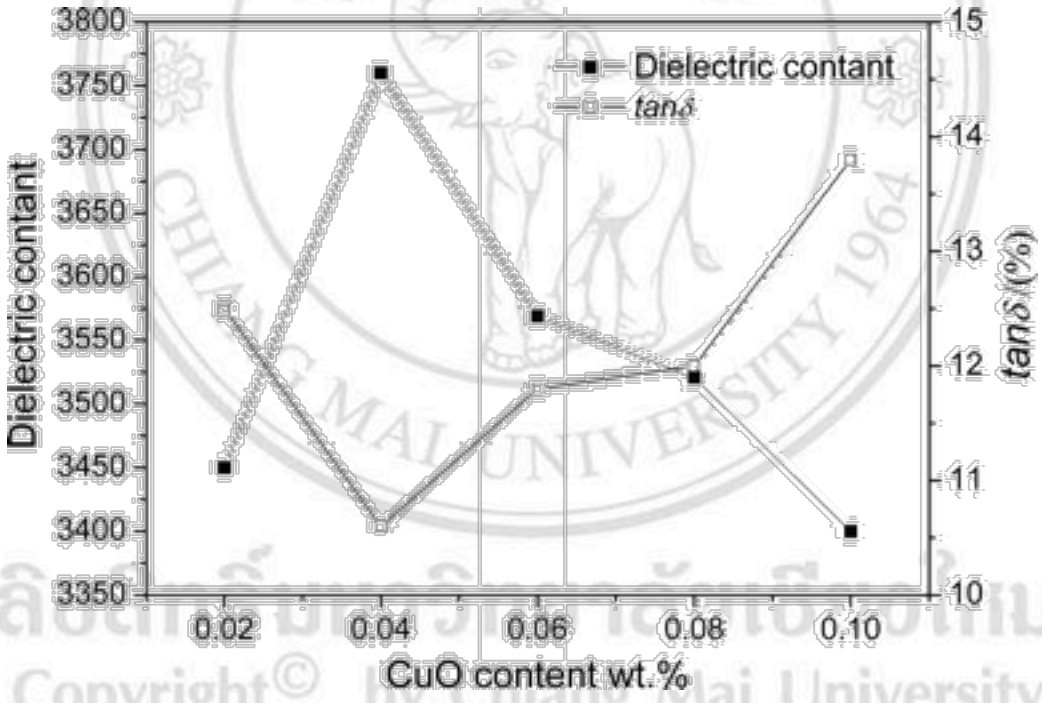

Figure 2.22 Dielectric properties of BCZT-*x*CuO ceramics [51].

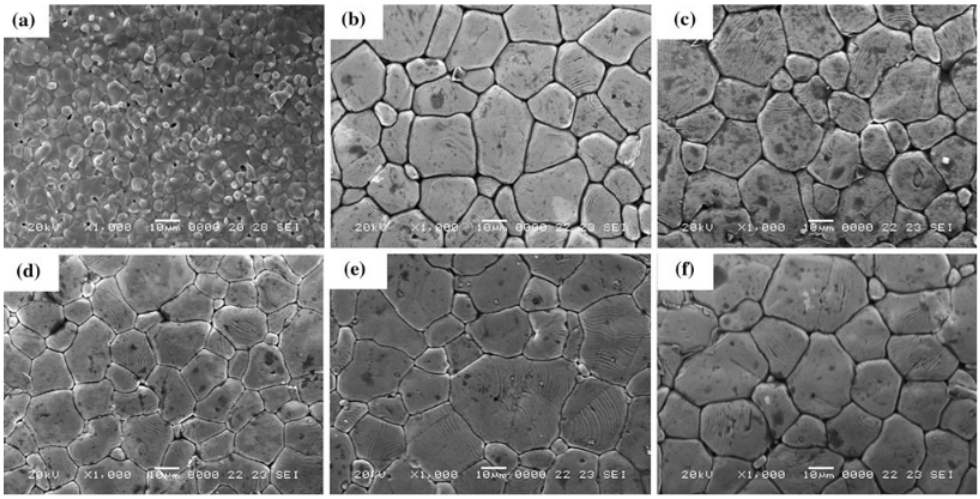

Figure 2.23 SEM micrographs of the BCZT-$x$$Y_2O_3$ ceramics [52].

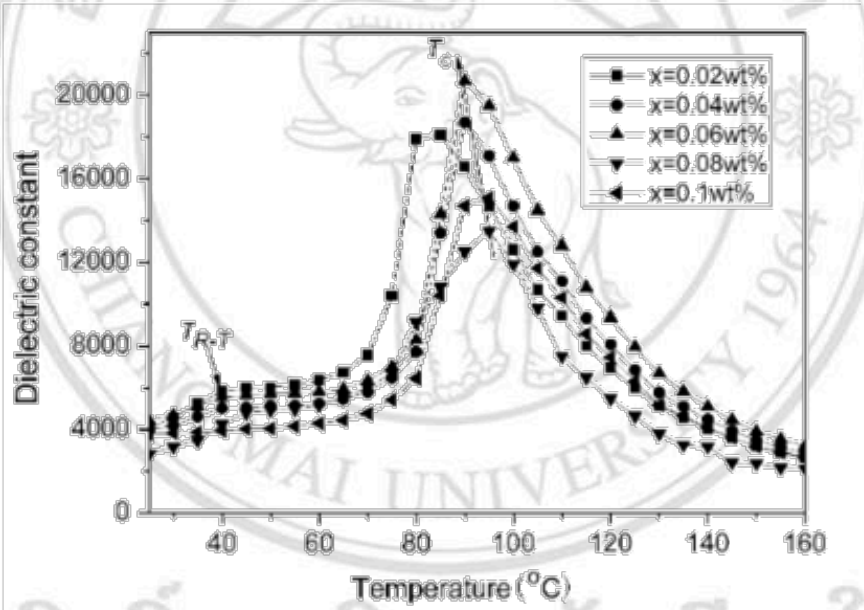

Figure 2.24 Temperature dependence of dielectric permittivity for the BCZT-$x$$Y_2O_3$ ceramics [52].

In 2016, Wang et al. observed the addition of Bi_2O_3/CuO into BCZT ceramics to form $(Ba_{0.85}C_{0.15-2x}Bi_{2x})(Zr_{0.1}Ti_{0.9-x}Cu_x)O_3$ [53]. The XRD patterns showed that the orthorhombic phase transformed to orthorhombic and tetragonal phases with increasing of Bi_2O_3 and CuO addition. The structure distortion by the difference in the ionic radius of Bi^{3+}(1.17Å) and Cu^{2+}(0.73Å) substituting into BCZT ceramics is shown in Fig.2.25 (a) and (b). The dielectric properties of $(Ba_{0.85}Ca_{0.15-2x}Bi_{2x})(Zr_{0.1}Ti_{0.9-x}Cu_x)O_3$ ceramics

are shown in Fig.2.26. The results presented that the T_C and ε_{max} decreased, while the diffuse phase transformation (DPT) increased with increasing Bi_2O_3 and CuO addition.

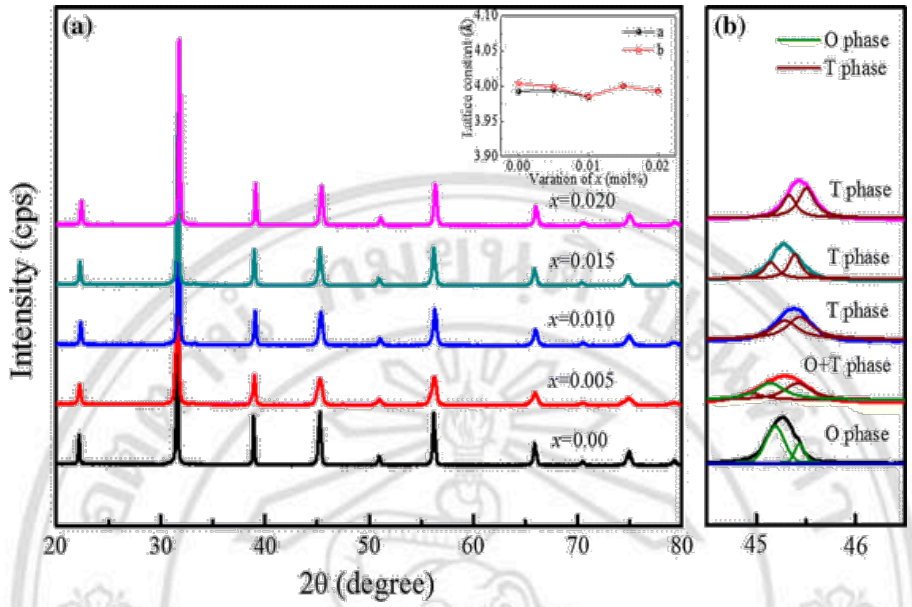

Figure 2.25 XRD patterns of $(Ba_{0.85}C_{0.15-2x}Bi_{2x})(Zr_{0.1}Ti_{0.9-x}Cu_x)O_3$ ceramic (a) 2θ = 20º-80º and (b) 2θ = 44º-47º [53].

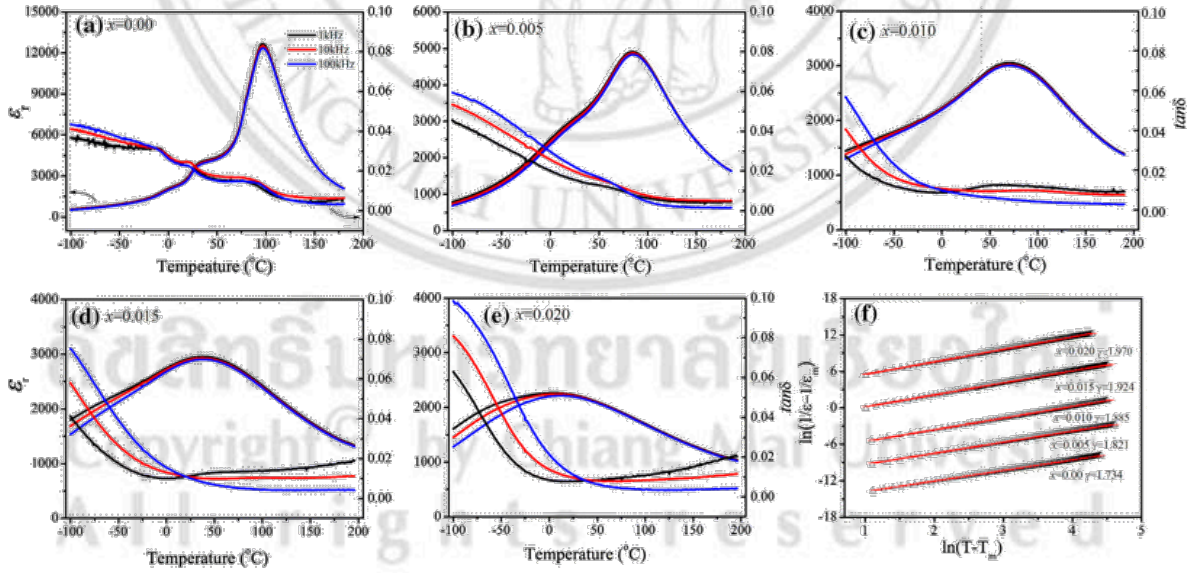

Figure 2.26 Dielectric properties and the plot of $\ln(1/\varepsilon - 1/\varepsilon_m)$ versus $\ln(T-T_m)$ of $(Ba_{0.85}C_{0.15-2x}Bi_{2x})(Zr_{0.1}Ti_{0.9-x}Cu_x)O_3$ ceramic [53].

Coondoo et al [54] studied Pr_2O_6-modified BCZT ceramics (BCZT-*x*Pr). They reported that the XRD patterns were refined using the GSAS software with the graphical interface

EXPGUI. Rietveld refinement of XRD patterns for composition with Pr < 0.05 wt% presented the combination of 2 structures, i.e. tetragonal and rhombohedral with space groups *P4mm* and *R3m* (R_{wp} = 8.54% and χ^2 = 6.23), respectively. On the other hand, for composition with Pr > 0.05 wt% showed good fit with tetragonal *P4mm* space group (R_{wp} = 7.99% and χ^2 = 5.68) in as seen Fig. 2.27. Dielectric properties exhibited that the addition of Pr in BCZT ceramics could increase in the peak value but did not influence the phase transition temperature (T_{R-T} and T_C) as shown in Fig.2.28.

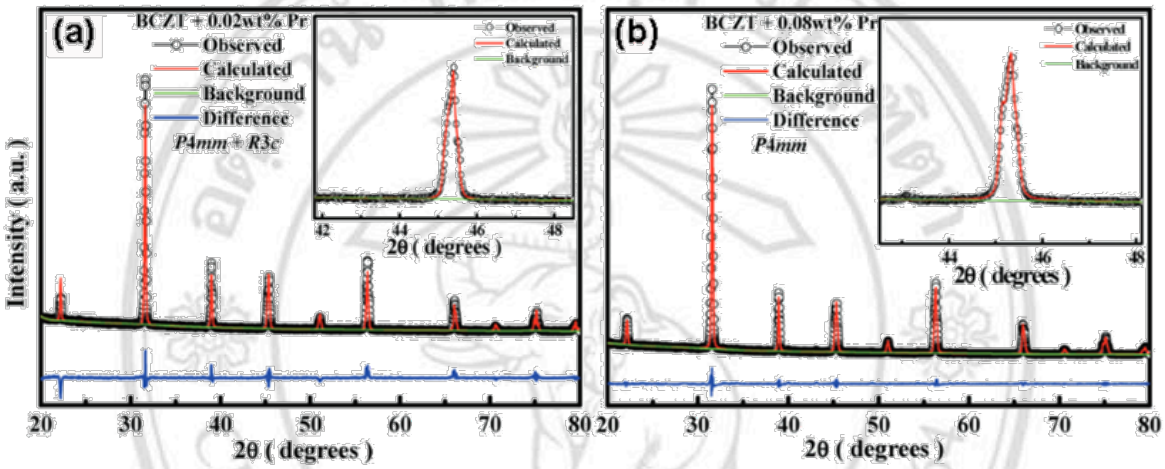

Figure 2.27 Rietveld refinement of XRD patterns for BCZT-*x*Pr (a) *x*=0.02wt% and (b) *x*=0.08wt% [54].

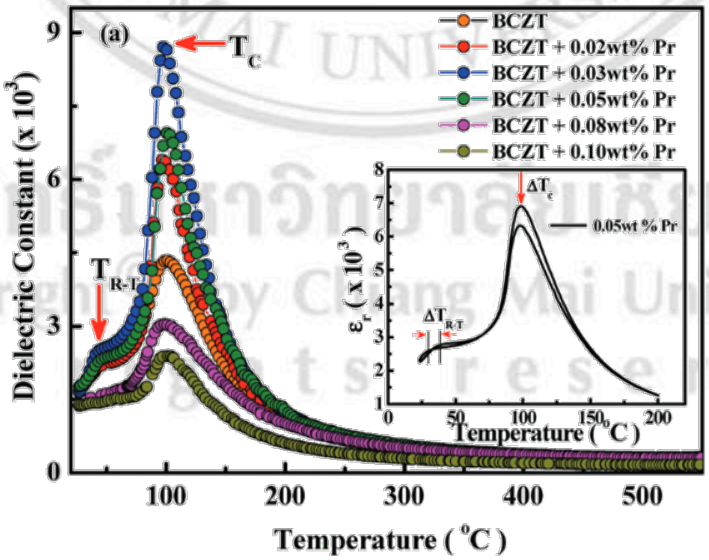

Figure 2.28 Temperature dependence of dielectric permittivity of BCZT-*x*Pr ceramics [54].

In 2016, Hayati et al [55] studied the addition of Bi_2O_3 (Bi) into the BCZT ceramics. The BCZT powder was calcined and it was added with different amount of Bi powder in the range of 0.05, 0.1, 0.5 and 1 mol%. The sample names for theses ceramics were BCZT, BCZT-0.05Bi, BCZT-0.1Bi, BCZT-0.5Bi and BCZT-1Bi. The mixtures were sintered from 1350-1500ºC for 4 h. The highest density was observed for the BCZT ceramic sintered at 1450ºC. The XRD patterns showed that the pure perovskite phase and no secondary were observed in all ceramics. The XRD results presented a slight tetragonal distortion by addition of Bi which showed that the peaks shifted backward to the low angles. These results indicated the incorporation of a larger Bi^{3+} cations (1.03 Å) than Zr^{4+} (0.70 Å) or Ti^{4+}(0.605 Å) cations as shown in Fig 2.29.

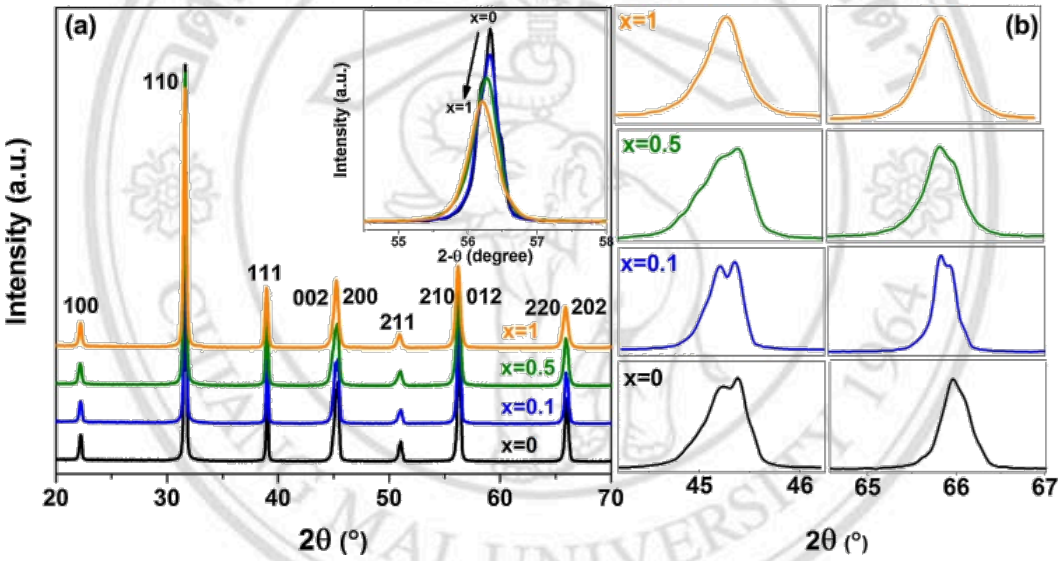

Figure 2.29 XRD patterns for BCZT-*x*Bi ceramics [55].

The SEM images of the BCZT-*x*Bi ceramics are shown in Fig. 2.30. The grain sizes decreased with increasing the amount of Bi powder which indicated that the Bi acted as liquid phase existed at grain boundaries and thus interrupted the growing grain. Figure 2.24 shows the temperature dependence of dielectric permittivity for BCZT-*x*Bi ceramics. The BCZT ceramic (Fig. 2.31 (a)) exhibited 3 peaks for the phase transition temperatures observed at 0ºC (R-O), 31ºC (O-T), and 91ºC (T-C). The transition temperature decreased from 100ºC (BCZT-0.1Bi), 75ºC (BCZT-0.5Bi) and 60ºC (BCZT-1Bi) as Bi content increased.

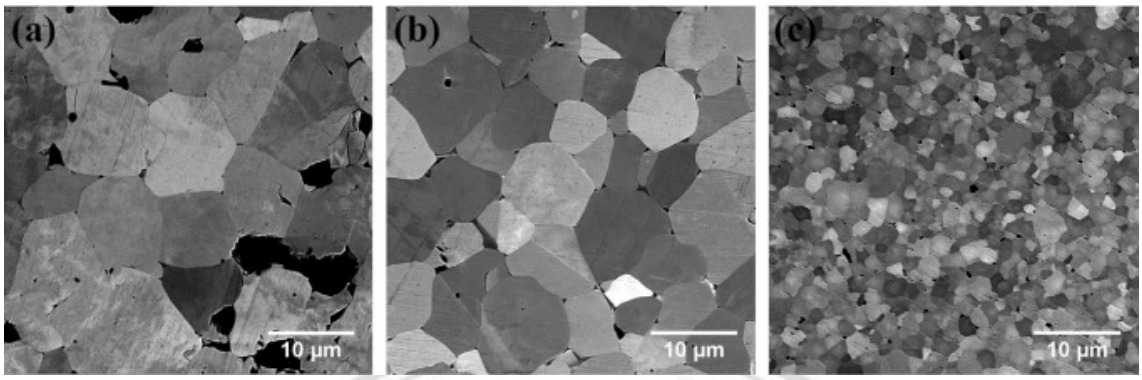

Figure 2.30 SEM images for BCZT *x*Bi ceramics with (a) $x = 0$, (b) $x = 0.1$ and (c) $x = 1$, respectively [55].

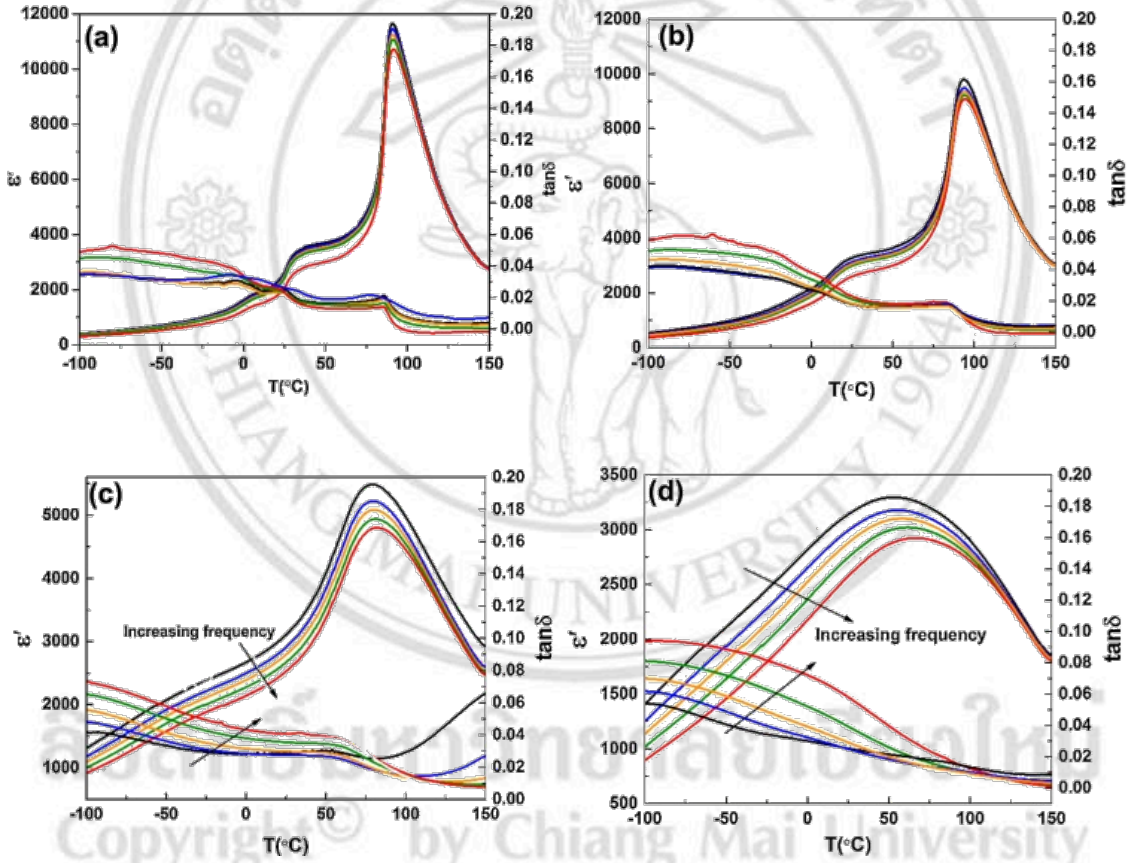

Figure 2.31 Temperature dependence of dielectric permittivity for BCZT-*x*Bi ceramics with (a) $x = 0$, (b) $x = 0.1$, (c) $x = 0.5$ and (d) $x = 1$, respectively [55].

Figure 2.32 presents the ferroelectric properties of BCZT-*x*Bi ceramics. The remnant polarization (P_r) decreased with increasing of Bi content from 11 μC/cm^2 for pure BCZT ceramic to 3 μC/cm^2 for BCZT-1Bi ceramic. They argued that the lower P_r was due to

difference of valence and ionic radius of Bi^{3+} ions in A-site and B-site ions which decreased in the long range ferroelectric order in the BCZT ceramics.

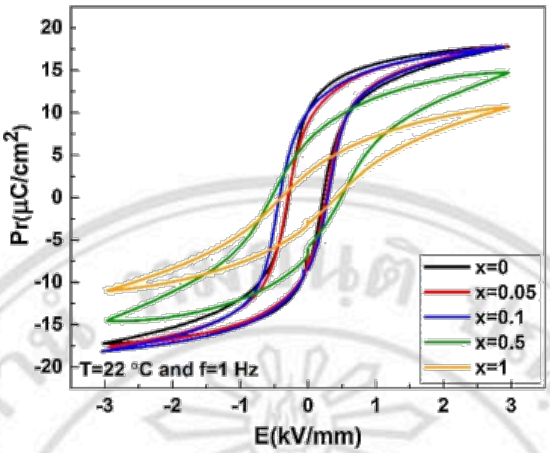

Figure 2.32 Hysteresis loops for BCZT-*x*Bi ceramics [55].

Moreover, another way to solving the high calcination and sintering temperatures are the nano-powder preparation because it requires the low heat energy. The details will be described in the following section.

2.5 Different powder preparation

In 2012, Wang et al [56] synthesized BCZT powder by a citrate sol-gel method FTIR patterns are shown in Fig. 2.33, O-H group (3440 cm^{-1}) was detected in BCZT gel and calcined powder (<600ºC) from water and citric acid. M-O-C (metal-oxygen-carbon), Zr-O and Ti-O showed peaks at 1452 cm^{-1} and 560 cm^{-1} which supported the XRD results in Fig.2.34. The Ba-O bonds at 517 cm^{-1} and 718 cm^{-1}, and Ti-O bonds at 257 $cm^{-1}$and 307 cm^{-1} were observed for BCZT calcined powder at 700ºC as shown in Fig.2.35.

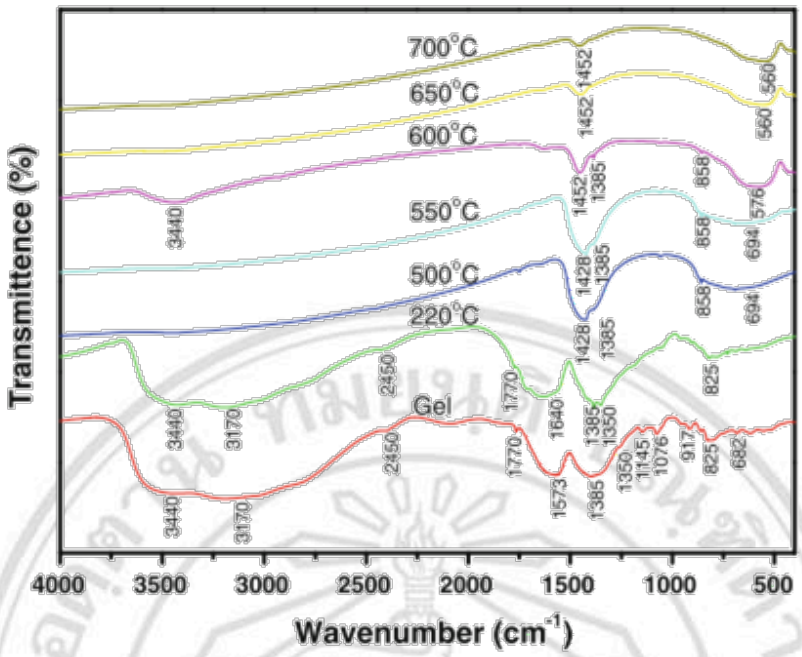

Figure 2.33 FTIR patterns of BCZT gel and powder at different calcination temperatures [56].

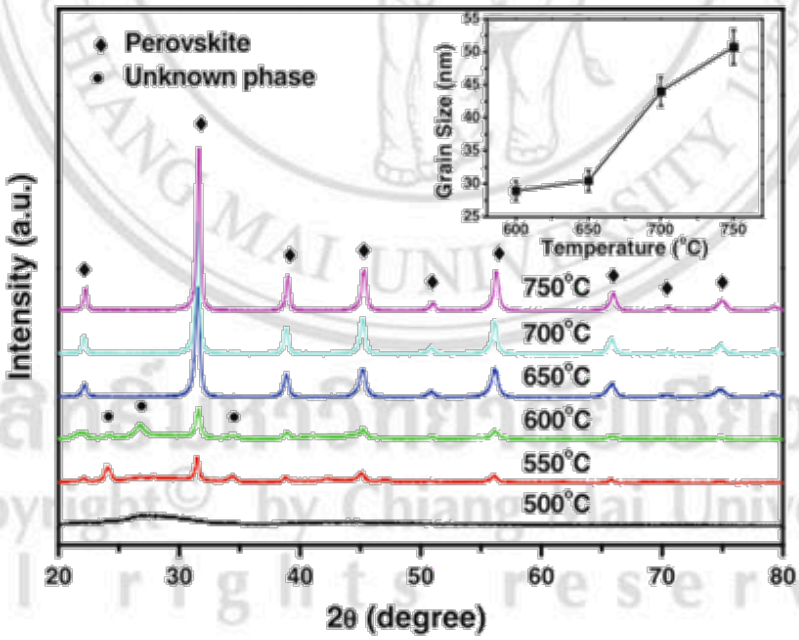

Figure 2.34 XRD patterns of BCZT gel and powder at different calcination temperatures [56].

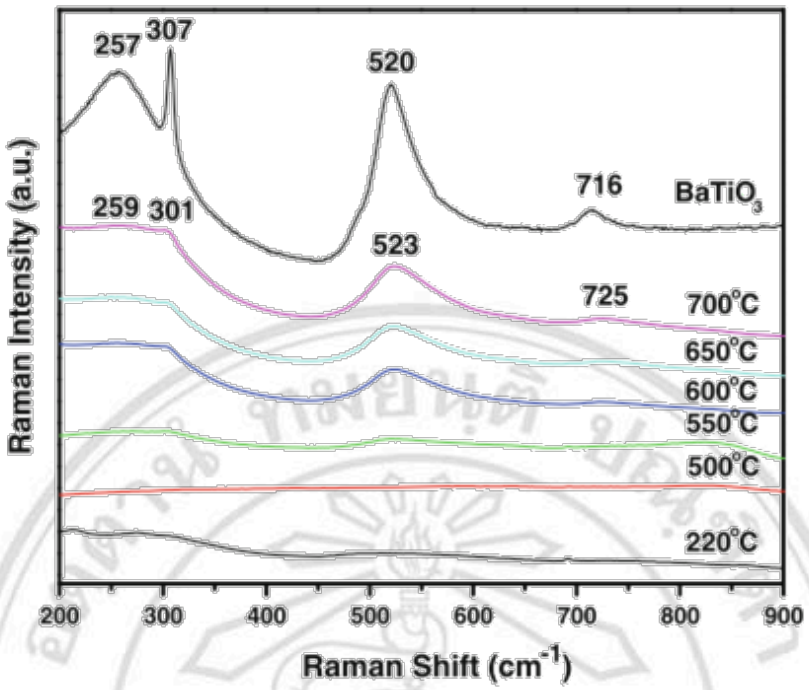

Figure 2.35 Raman patterns of BCZT gel, powder at different calcination temperatures and $BaTiO_3$ powder calcined at 700ºC [56].

The synthesis of BCZT nanopowder by solution based auto combustion was reported by Sahoo et al [57]. They found that, the BCZT powder calcined above 500ºC showed pure perovskite without impurity phases. The XRD patterns were fitted using a combination of 2 phases (tetragonal (*P4mm*) and orthorhombic (*Amm2*)). Figure 2.36 presents the FTIR spectra of BCZT powder at various calcination temperatures. The result showed that the nitrate and carboxylate were observed in the as-burnt powder while it disappeared at high calcination temperature around 700ºC. The vibration at peaks of Zr-O and Ti-O were found and confirmed the presence of perovskite structure in agreement with XRD patterns. They also found that the average size of BCZT powder was in the range of 40-70 nm (Fig.2.38). The Raman spectrum was obtained for the BCZT powder calcined at 700ºC. The tetragonal and orthorhombic peaks were obtained which could be indexed by the bands at 180 cm^{-1},190 cm^{-1}, 296 cm^{-1}, 520 cm^{-1} and 720 cm^{-1}, respectively.

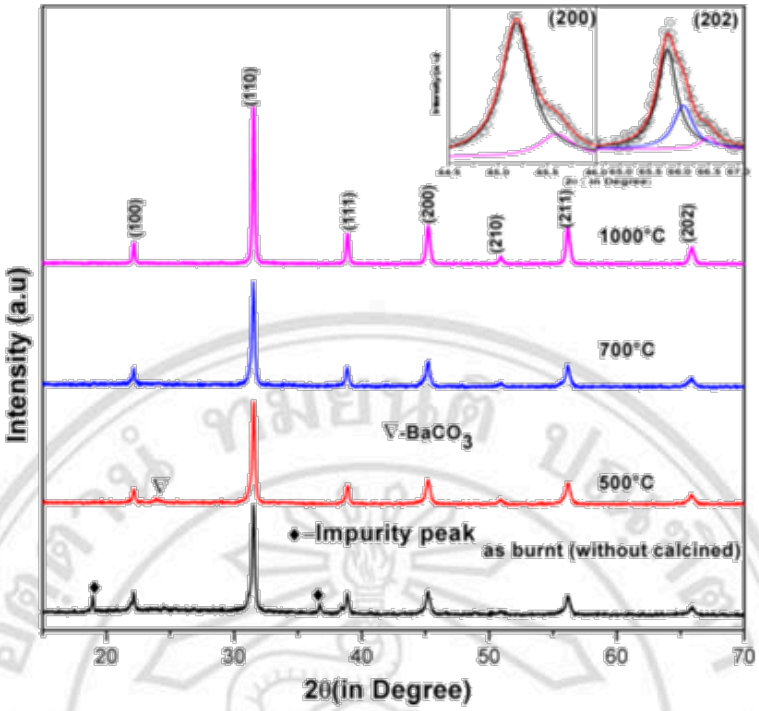

Figure 2.36 XRD patterns of BCZT powder calcined at different temperatures and enlarge peak at (200) and (202) [57].

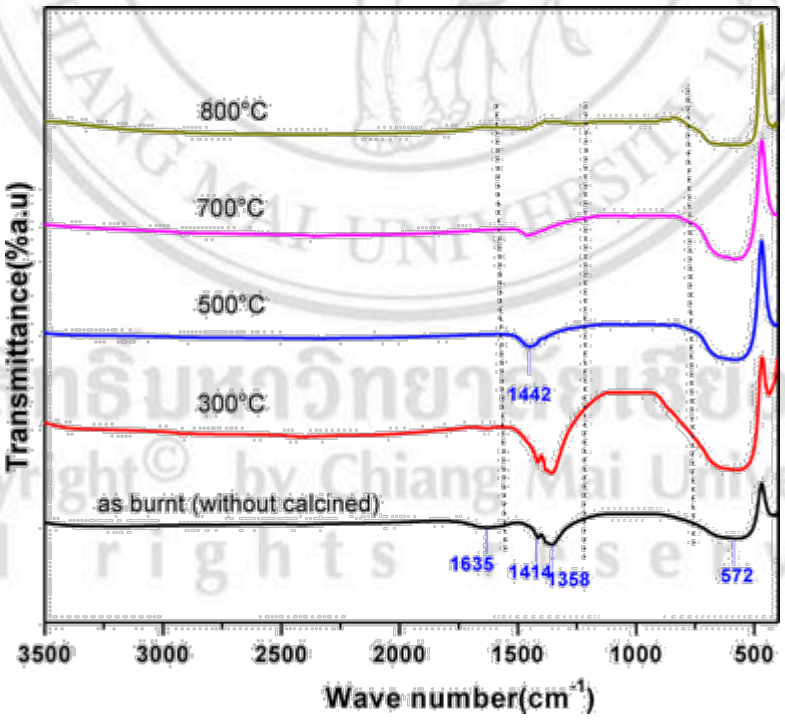

Figure 2.37 FTIR spectra of BCZT powder at various calcination temperatures [57].

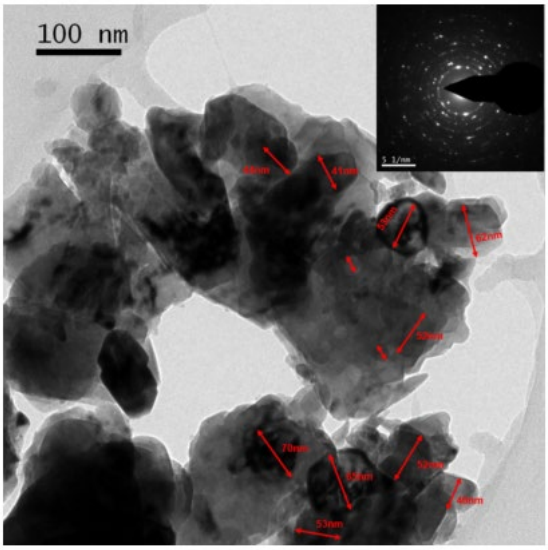

Figure 2.38 TEM image and selected area electron diffraction pattern of BCZT powder calcined at 700ºC [57].

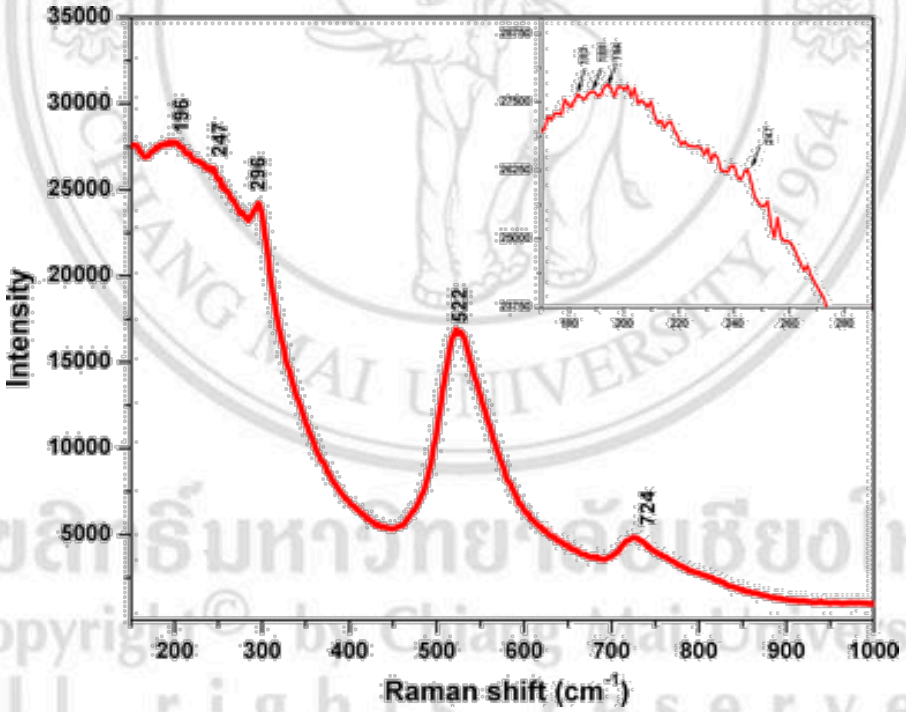

Figure 2.39 Raman spectra of the BCZT powder calcined at 700 ºC [57].